AGU PUBLICATIONS

JGR

Journal of Geophysical Research: Solid Earth

RESEARCH ARTICLE
10.1002/2015JB012321

Key Points:
- Literature is full of inconsistencies on HS-LS crossover in ferropericlase
- Demonstration of deviatoric stress and its effect on HS-LS crossover
- Demonstration of stresses on microlevel and their effect on HS-LS crossover

Supporting Information:
- Supporting Information S1

Correspondence to:
K. Glazyrin,
konstantin.glazyrin@gmail.com

Citation:
Glazyrin, K., N. Miyajima, J. S. Smith, and K. K. M. Lee (2016), Compression of a multiphase mantle assemblage: Effects of undesirable stress and stress annealing on the iron spin state crossover in ferropericlase, *J. Geophys. Res. Solid Earth*, *121*, 3377–3392, doi:10.1002/2015JB012321.

Received 13 AUG 2015
Accepted 8 MAY 2016
Accepted article online 13 MAY 2016
Published online 30 MAY 2016

Compression of a multiphase mantle assemblage: Effects of undesirable stress and stress annealing on the iron spin state crossover in ferropericlase

Konstantin Glazyrin[1,2], Nobuyoshi Miyajima[3], Jesse S. Smith[4], and Kanani K. M. Lee[1]

[1]Department of Geology and Geophysics, Yale University, New Haven, Connecticut, USA, [2]FS-PE Group, DESY-Deutsches Elektronen-Synchrotron Ein Forschungszentrum der Helmholtz-Gemeinschaft, Hamburg, Germany, [3]Bayerisches Geoinstitut, Universität Bayreuth, Bayreuth, Germany, [4]High Pressure Collaborative Access Team, Geophysical Laboratory, Carnegie Institution of Washington, Argonne, Illinois, USA

Abstract Using synchrotron-based X-ray diffraction, we explore characteristic signatures for nonhydrostatic stresses and their effect on the spin state crossover of ferrous iron in (Mg, Fe)O ferropericlase (Fp) upon compression in a two-phase mixture which includes an Al- and Fe-bearing bridgmanite (Bm). We observe an influence of nonhydrostatic stresses on the spin state crossover starting pressure and width. The undesirable stresses discussed here include uniaxial deviatoric stress evolving in the diamond anvil cell and effects of intergrain interaction. While the former leads to a pressure overestimation, the latter one lowers the pressure of the onset for the high-spin to low-spin electronic transition in Fe^{2+} in ferropericlase (Mg, Fe)O with respect to hydrostatic conditions.

1. Introduction

The Earth's lower mantle, which comprises most of the planet's volume and thus controls its thermochemical evolution, is thought to be dominated by two minerals, a magnesium silicate perovskite called bridgmanite (nominally (Mg,Fe,Al)(Si,Fe,Al)O_3) and ferropericlase (nominally (Mg,Fe)O) [*Lee et al.*, 2004; *Xu et al.*, 2008; *Tschauner et al.*, 2014]. The properties of bridgmanite (Bm) and ferropericlase (Fp) (e.g., equation of state, partitioning, and melting behavior), have long been studied to infer the physical and chemical properties of the Earth's lower mantle. After decades of extensive research, we have begun to understand the role of minor elements, especially, the role of iron.

The discovery of the electronic spin state transition of iron (both ferrous Fe^{2+} and ferric Fe^{3+}) in Fp and Bm opens a new page for studies investigating the deep Earth [*Badro et al.*, 2003; *Lin et al.*, 2013]. Both pressure (*P*) and temperature (*T*) induce changes in the distribution of 3*d* electrons between the electronic orbitals of Fe incorporated into the lower mantle minerals and promote changes of elastic properties [*Lin et al.*, 2005; *Sturhahn et al.*, 2005; *Marquardt et al.*, 2009; *Antonangeli et al.*, 2011; *Chen et al.*, 2012] as well as affect transport properties of the lower mantle minerals [*Hsu et al.*, 2010; *Potapkin et al.*, 2013]. Previous studies have found that the pressure and temperature conditions change the crystal chemistry of Bm promoting redistribution of minor elements (e.g., Al) between different crystallographic sites accompanied by a spin state crossover of ferric iron in Bm [*Catalli et al.*, 2010, 2011]. Moreover, a spin state crossover of ferrous iron may change iron partitioning between lower mantle phases [*Badro et al.*, 2003; *Irifune et al.*, 2010]. In Fp, the second most abundant phase of the Earth's lower mantle pressure induces a Fe^{2+} high-spin (HS) to low-spin (LS) transition.

Previous studies highlight the importance and complexity of different phenomena related to spin state crossover in either Bm or Fp as well as the importance of the phases for our understanding of planetary interiors. We focus on the behavior of Fp and note that even after more than a decade of research focused on a spin state crossover in Fp ($Mg_{1-x}Fe_xO$), we find many discrepancies with the phase diagram of Fp HS-LS spin state crossover as a function of iron content, even at room temperature. We review many of the previous publications and provide a detailed description of pressure media, stress state, and iron content and their effects on the spin state crossover starting pressure and the broadness of this transition (Table 1). The list assembled in Table 1 cannot not be considered complete, and for additional references we direct to the review of *Lin et al.* [2013].

As shown in Figure 1, we demonstrate the magnitude of inconsistencies in the literature regarding critical pressures (start and end) for spin state crossover, especially for compositions relevant for the Earth's lower mantle

Table 1. Experimental Details of Iron Spin State Crossover in Fp ($Mg_{1-x}Fe_xO$) Phases[a]

Reference	x	Sample Type	Experiment	Pressure Medium	Density Estimation	Crossover Detection	Sample Annealing
Crowhurst et al. [2008]	0.06	S.C.	DAC	Ar	indirect[b]	ISLS, elast. moduli	No
Marquardt et al. [2009][c]	0.10	S.C.	DAC	MEW, Ar, Ne	indirect[d]	Brillouin, elast. moduli	No
Marquardt et al. [2009][c]	0.10	PWDR	DAC	Ne	in situ	XRD	No
Irifune et al. [2010]	0.11	PWDR Bm + Fp	MA	-	-	K_D change	Yes
Badro et al. [2003]	0.17	PWDR	DAC	Fp	-	XES	No
Lin et al. [2005]	0.17	PWDR	DAC	Ne	in situ	XRD	No
Antonangeli et al. [2011]	0.17	S.C.	DAC	Ne	in situ	IXS, elastic moduli	No
Fei et al. [2007a]	0.2	PWDR	DAC	NaCl	in situ	XRD	Yes
Lin et al. [2005]	0.25	S.C.	DAC	NaCl	-	XES	No
Mao et al. [2011]	0.25	PWDR	DAC	KCl, NaCl[e]	in situ	XRD	Yes
Chen et al. [2012]	0.35	PWDR	DAC	Ne	in situ	XRD	No
Fei et al. [2007a]	0.39	PWDR	DAC	NaCl	in situ	XRD	Yes
Zhuravlev et al. [2009]	0.39	PWDR	DAC	Ne	in situ	XRD	No
Fei et al. [2007a]	0.58	PWDR	DAC	NaCl	in situ	XRD	Yes
Lin et al. [2005]	0.60	S.C.	DAC	NaCl	-	XES	No

[a]Unless stated otherwise, the sample material consists of only the Fp phase. Our estimates of the spin state crossover pressures are listed based on our reanalysis of F-f_E data (Figure S1). S.C., single crystal; PWDR, powder; MA, multianvil apparatus; DAC, diamond anvil cell; MEW, mixture methanol:ethanol:water, 16:3:1 volume ratio; $K_D = (Fe/Mg)_{Mg\text{-}Bm}/(Fe/Mg)_{Mw}$, iron partitioning coefficient between Bm and Fp. ISLS, impulsive stimulated light scattering (laser-based acoustic wave excitation); XRD, X-ray diffraction; XES, X-ray emission spectroscopy; IXS, inelastic X-ray scattering technique.
[b]Densities at high pressure were iteratively determined from the measured velocities and initial density.
[c]Brillouin single-crystal and powder diffraction studies are consistent (see Text S1 in supporting information). For estimation of Fp spin state crossover region we rely on powder diffraction data.
[d]Density was estimated from powder X-ray diffraction data collected separately and published in the same study.
[e]KCl was used for experiments below 60 GPa, NaCl for experiments above 60 GPa.

(Fp $x_{Fe} \approx 0.2$) [e.g., *Badro et al.*, 2003; *Bina*, 2005; *Lin et al.*, 2005; *Fei et al.*, 2007a; *Antonangeli et al.*, 2011]. We also find notable contradictions appearing for studies focused on similar materials ($x = 0.35, 0.39$) [*Zhuravlev et al.*, 2009; *Chen et al.*, 2012] conducted under seemingly similar quasi-hydrostatic conditions (Table 1). The inaccuracy of Fp iron spin state crossover determination prevents creation of realistic models describing elastic properties for the Earth's lower mantle and interiors of extraterrestrial planetary bodies based on similar chemistry.

In this study we address the problem of Fp spin state crossover phase diagram. We compress a Bm + Fp mixture (synthesized in a multianvil press) at conditions close to hydrostatic (S1) and at nonhydrostatic conditions (S2). By making the deliberate choice of a multiphase system containing, similar to that of Earth's interior, the stiffer Bm and softer Fp, we study their simultaneous compression, spin state crossover, and the effects of nonhydrostatic conditions by means of X-ray diffraction (XRD). It should be noted that due to various reasons, including the abundant existing literature on chemistry of lower mantle materials and, in particular, the element partitioning, we need a deeper understanding of the character and features of multiphase compression from an experimental point of view.

Following recent publications [e.g., *Dorfman et al.*, 2012], we demonstrate that employing a soft hydrostatic pressure medium (Ne) provides no warranty against the evolution of undesirable stresses. We present a case study of a complex multiphase system and demonstrate the experimental manifestation and the magnitude of undesirable stresses on the spin state crossover of iron in ferropericlase with respect to our and literature data. The complexity of the studied system is strongly related to its initial state (dense sintered) and contrasting elastic properties of multiphase constituents, e.g., the contrast of hardness. Additionally, we discuss signatures specific to the manifestation of nonhydrostatic stresses in a typical XRD diamond anvil cell (DAC) experiment with the compression axis coinciding with the X-ray beam. Finally, we focus on the XRD technique because this method carries the inherent information on density. Review of the literature shows that most of the time this crucial information is missing for data measured by other techniques, e.g., various spectroscopy (Mössbauer in energy and time domains, Brillouin, etc.; for a recent review please see *Lin et al.* [2013]).

2. Methods

2.1. Material Synthesis

A mixture of Fp and Bm phases was synthesized in a KIWI 1000 t Kawai-type multianvil apparatus at Yale University from glass prepared using the laser levitation method. The glass was loaded into a capsule (Au-Pd—75 wt % Au,

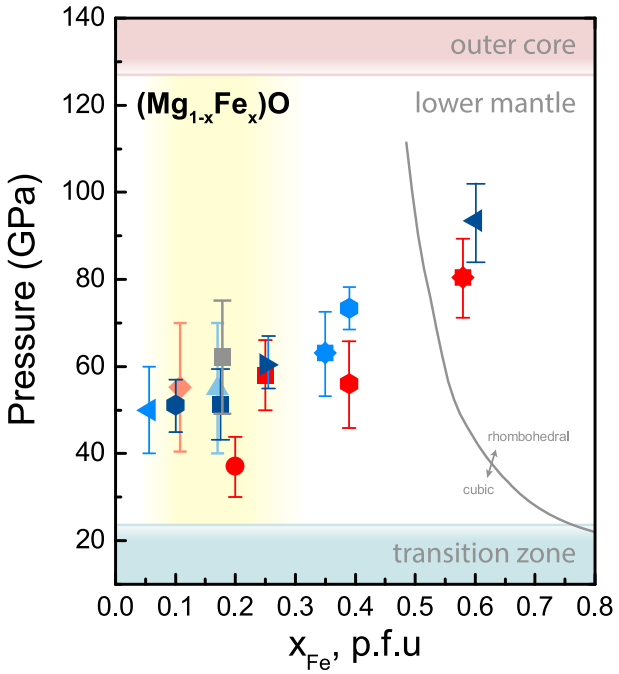

Figure 1. Phase diagram of ferropericlase ($Mg_{1-x}Fe_xO$) demonstrating literature data on spin state crossover. All data points were measured at room temperature. Listing from left to right: light blue left triangle $x = 0.06$ [*Crowhurst et al.*, 2008]; dark blue hexagon $x = 0.1$ [*Marquardt et al.*, 2009]; light red diamond $x = 0.11$ [*Irifune et al.*, 2010]; light blue triangle $x = 0.17$ [*Antonangeli et al.*, 2011]; dark blue square $x = 0.17$ [*Lin et al.*, 2005]; gray square $x = 0.17$ [*Badro et al.*, 2003]; red circle $x = 0.2$ [*Fei et al.*, 2007a]; red square $x = 0.25$ [*Mao et al.*, 2011]; dark blue right triangle $x = 0.25$ [*Lin et al.*, 2005]; light blue star $x = 0.35$ [*Chen et al.*, 2012]; red hexagon $x = 0.39$ [*Fei et al.*, 2007a]; light blue hexagon $x = 0.39$ [*Zhuravlev et al.*, 2009]; dark blue left triangle $x = 0.4$ [*Lin et al.*, 2005]; red star $x = 0.58$ [*Fei et al.*, 2007a]. Symbols painted in red indicate sample annealing, while symbols painted in blue and gray indicate absence of temperature treatment. In contrast to all other symbols indicating measurement on powders, the triangles indicate single-crystal loadings. Error bar symbols correspond to the apparent width of the transition. Additional details and figures on literature data and spin state crossover region determination can be found in Table 1 as well as in Figure S1 in the supporting information. Solid gray line highlights a compression-induced crystal lattice transition [*Fei et al.*, 2007a]. By using blue, white, and red gradient regions, we highlight pressure ranges corresponding to the Earth's transition zone, lower mantle, and outer core [*Dziewonski and Anderson*, 1981]. Region with yellow gradient corresponds to the compositions of Fp considered the most probable for the Earth's lower mantle.

25 wt % Pd) inserted into a Cr-doped MgO octahedron and heated for 2.5 h at 1805(11) K at 25 GPa according to the previously established relations between electric power and temperature generated by $LaCrO_3$ heater. The short synthesis time produced small grains (≤1 μm) ideal for XRD measurements (supporting information Figure S2). The choice of the grain size should satisfy the following requirements: grains should be large enough to prevent significant modification of properties by effects of grain surfaces (nano regime) but at the same time provide enough statistics for powder XRD signal.

2.2. Material Characterization

2.2.1. Electron Probe Microanalyses

The bulk composition of the synthesized sample (K1297) was fully characterized by Electron Probe Micro Analyzer (EPMA, JEOL JXA-8530F) using a 10 kV and 25 μm beam size (Table 2).

According to our EPMA data, the composition of our starting sample K1297 is similar to a "pyrolite" composition [*Ringwood*, 1975]; however, it also bears specific features of the *Javoy et al.* [2010] model, namely, lower Al and higher Si and Fe concentrations (Table 2). Higher iron content is also important, as it increases the sensitivity of the spin state crossover detection with XRD. We note that in the variety of the models describing the composition of the silicate Earth, the model of "pyrolitic" unified silicate mantle and the model of layered silicate mantle proposed by *Javoy et al.* [2010] are considered the most probable.

Table 2. We Compare Our Bulk Composition of K1297 Sample Material (Multianvil Synthesis) With Model Lower Mantle Compositions: Homogeneous Silicate Mantle of the Earth (i.e., Pyrolite), Lower Mantle Model of the Earth Formed From Enstatite Chondrites[a]

Mg	Si	Al	Ca	Fe	Ni	Reference
23.0	21.1	1.75	2.21	6.22	–	Pyrolite [*Ringwood*, 1975]
21.3 (7)	24.2 (5)	1.0 (4)	1.0 (4)	7.2 (4)	0.2 (2)	Enstatite Chondrite LM [*Javoy et al.*, 2010]
22.9 (1)	22.6 (2)	1.1 (0)	1.1 (0)	7.7 (4)	0.1 (1)	Current study (K1297)

[a]Data are shown in wt % with balance due to oxygen. *Javoy et al.* [2010] composition was renormalized, reflecting the negligible contributions from minor elements (S, Ti, Cr, and Co).

2.2.2. Individual Phase Compositions

The composition of 10 Bm and 8 Fp grains of the K1297 material was further clarified in a TEM-EDXS study (transmission electron microscope-energy dispersive X-ray spectroscopy). EDXS spectra were collected with 60 s live time and were quantified by the absorption correction according to the generally accepted approach [*Van Cappellen and Doukhan*, 1994]. The method is corrected for X-ray absorption on the basis of the principle of electron neutrality and requires the quantification of oxygen. The *k* factors were calibrated, using the parameterless correction method [*Van Cappellen*, 1990]. The average composition of Bm is $Mg_{0.89(3)}Fe_{0.09(1)}Ca_{0.02(1)}Si_{0.96(3)}Al_{0.04(3)}O_3$, which is consistent with the general notion that at relatively low synthesis pressures (~25 GPa), Fe^{3+} tends to be charge coupled with Al^{3+} in the A and B sites, respectively of the crystal lattice of Bm. The TEM analysis measures $Mg_{0.76(2)}Fe_{0.24(2)}Si_{0.01(0)}O$ for the Fp phase composition, which corresponds to a ferrous iron partitioning coefficient $K_D = (x_{Fe}^{2+}/x_{Mg})_{Bm}/(x_{Fe}^{2+}/x_{Mg})_{Fp} = 0.17(4)$. This value is in good agreement with data on ferrous iron partitioning between Bm and Fp phases (e.g., from San Carlos olivine precursor) [*Kobayashi*, 2005].

In order to improve our estimate of ferric iron abundance in the synthesized Bm and Fp, we conducted an electron energy-loss spectroscopy (EELS) study on an Ar ion milled sample using a 200 kV analytical scanning transmission electron microscope (TEM, Philips CM20FEG) equipped with a parallel electron energy-loss spectrometer (PEELS, Gatan 666) as well as Mössbauer spectroscopy at Bayerisches Geoinstitut.

To minimize electron irradiation damage during EELS measurements, the TEM thin foil was cooled to nearly liquid nitrogen temperature (approximately 105 K) in a Gatan cooling stage. The analysis of Fe-$L_{2,3}$ energy-loss near-edge structure (ELNES, Figure S3, supporting information) [*van Aken and Liebscher*, 2002] provides the following information for Fp: $Fe^{3+}/\Sigma Fe = 9(7)\%$. The quality of ELNES spectra for Bm is low, due to lower iron abundance; however, we find the $Fe^{3+}/\Sigma Fe$ value provided by the method reasonable: 57(4)%. This value is further clarified by Mössbauer analysis.

^{57}Fe Mössbauer spectrum was recorded at ambient conditions in transmission mode on a constant acceleration Mössbauer spectrometer with a nominal 370 MBq ^{57}Co high specific activity source embedded in a 12 μm thick Rh matrix. The full description of methodology can be found elsewhere [*McCammon*, 1992; *Kantor et al*., 2004]. The velocity scale was calibrated relative to 25 μm thick α-Fe foil.

The Mössbauer spectrum was fitted employing Lorentzian spectral response functions (Figure S4). We calculated the relative subspectra contributions with respective Mössbauer parameters, namely, IS and QS represent isomer shift and quadrupole splitting Mössbauer parameters, respectively. Different Bm Fe^{2+} contributions were fit using a single width. We also imposed a separate single-width constraint on Fe^{2+} and Fe^{3+} contributions of Fp as well as fixed isomer shift of Fe^{3+} Fp contribution to a reasonable value of 0.13 mm/s relative to the iron calibration foil [*Otsuka et al*., 2010]. Considering relative abundance of ferric and ferrous iron in the synthesized Bm phase and our EELS data collected on Fp, for Bm material we report the following value: $Fe^{3+}/\Sigma Fe = 49(5)\%$. Areas corresponding to Bm and Fp phases have, respectively, the following contributions to the total Mössbauer signal: 57.6 ± 1.9% and 42.4 ± 2.2%. Considering different volume abundances of the phases (Figure S2), we conclude that Fp phase has higher iron content, consistent with the TEM-EDXS measurements. The fit was further constrained by setting Fe^{3+} Fp subspectrum area to the value of 9% of Fe^{2+} Fp contribution. The Mössbauer parameters derived from the fit are reported in more detail in the supporting information (Table S1 and Figure S4).

2.2.3. High-Pressure X-Ray Diffraction Experiments

High-pressure XRD studies were conducted at beamline 16-IDB, High Pressure Collaborative Access Team (HPCAT), at the Advanced Photon Source (APS). We used symmetric DACs with 200 μm culet diamond anvils. Samples were loaded into Re gaskets with 100 μm diameter holes precompressed to a thickness of 30 and 36 μm (samples S1 and S2, respectively, Figure 2). We used Ne gas as a pressure medium and as thermal insulation (GeoSoilEnviroCARS gas loading system, APS). It is generally accepted that Ne is one of the best pressure media in terms of attained hydrostatic conditions [*Klotz et al*., 2009] and pressure chamber stability upon laser heating. X-ray diffraction (beam size 6 × 6 μm^2) was collected on a MAR345 image plate using the X-ray wavelength $\lambda = 0.3738$ Å.

Although the starting compositions of S1 and S2 are identical, there is an evident difference in their preparation and dimensions (Figure 2). While S1 was prepared by crushing the multianvil synthesized material in an agate mortar, S2 was prepared by gentle polishing of the same material to a thickness of ~15 μm.

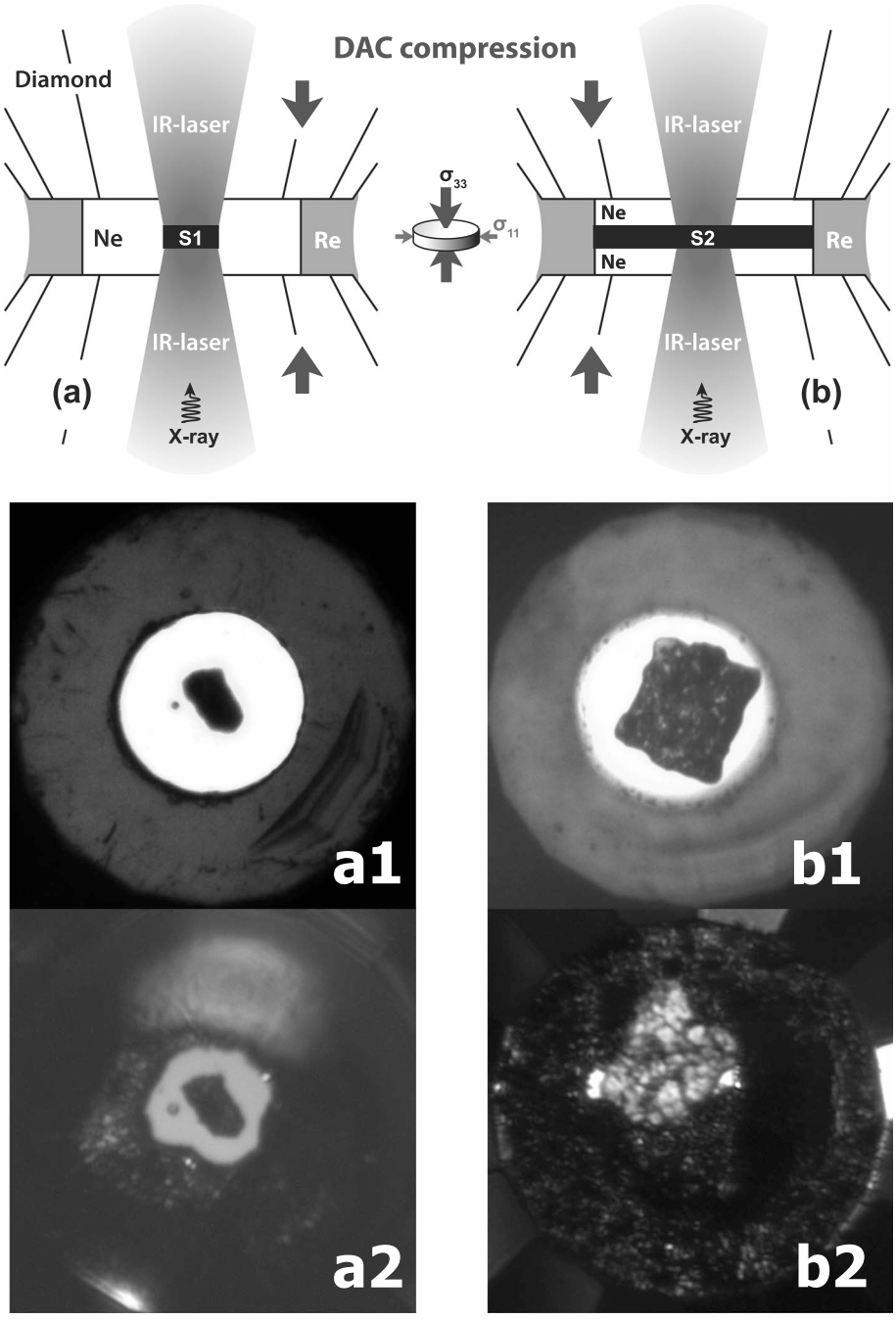

Figure 2. Simplified diagrams of the experiments and photographs of the sample. (a) In case of S1 we have a sample completely surrounded by Ne. (b) S2 almost completely covers the sample chamber promoting evolution of the deviatoric stress component. S2 sample is surrounded by Ne from the top and the bottom. The image placed between Figures 2a and 2b shows a simple stress diagram representing both cases. For S1, we have approximately $\sigma_{33} = \sigma_{11}$ and $|\sigma_{33}| > |\sigma_{11}|$ for S2, respectively, where $|\sigma_{ij}|$ corresponds to the absolute value of the stress component. The compression axis of the diamond anvils coincides with the direction of the incoming X-ray diffraction beam employed for data collection. We employed double-sided laser heating. Below the diagrams we demonstrate the different stages of the experimental loading for samples (a1, a2) S1 and (b1, b2) S2. Figures 2a1 and 2b1 correspond to a stage preceding Ne gas loading to sample chamber, while Figures 2a2 and 2b2 correspond to a stage of full sample decompression. Figure 2b2 suggests higher sample hardness than that of the Re gasket and supports our hypothesis of nonnegligible deviatoric stress component evolution during compression.

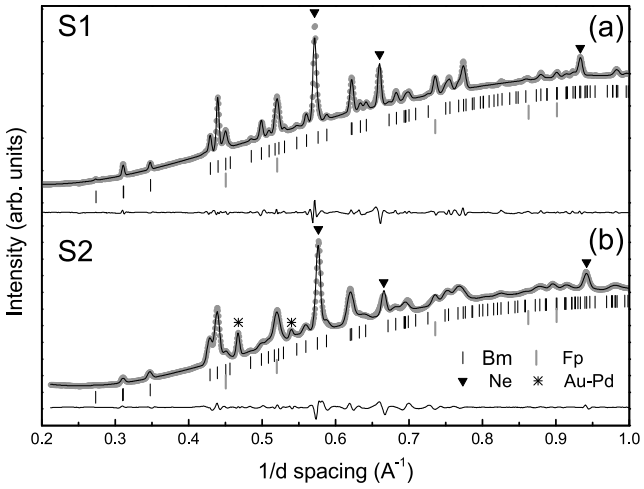

Figure 3. X-ray diffraction patterns collected at ambient temperature after sample laser annealing for (a) S1 and (b) S2 samples. Different symbols shown in the figure represent diffraction positions of various solids present in the sample chamber, namely, (black ticks) Bm, (grey ticks) Fp, (black triangle) Ne, and (star) Au-Pd. Black line passing through the light grey data points corresponds to LeBail fit of the data. Note considerable broadening in case of S2 and considerable amount of Ne phase detected in each case. Patterns in Figures 3a and 3b were collected at 79 GPa and 88 GPa (Ne pressure scale), respectively. Residuals of the fit are shown with a thin line.

In addition to the roles of a pressure medium and thermal insulation, we used Ne as a pressure standard [*Fei et al*., 2007b]. However, in order to facilitate Ne gas loading and for measurements conducted below the Ne solidification pressure (4.6 GPa at 300 K) [*Shimizu et al*., 2005], we also employed small spheres of ruby as a pressure standard [*Mao et al*., 1986]. A small amount of Au-Pd material was incorporated into the S2 sample material at the stage of synthesis, and we found it to be a useful secondary indicator of S2 stresses and discuss the topic below. For pressure determination using Au-Pd alloy as a standard and assuming Vegard's rule, we employ the following parameters: $K_0^{\text{Au-Pd}} = 176.5$ GPa, $V_0^{\text{Au-Pd}} = 64.29$ Å^3, and $K'^{\text{Ad-Pd}} = 5.5$ (see supporting information for details).

In the course of our investigation, we employed double-sided laser heating to anneal the samples at high *P-T* conditions [*Meng et al*., 2006]. The laser system has the following characteristics: full width at half maximum of the laser heating spot is ~34 μm with a flat-top power distribution. It has been shown that homogeneous heating is the key for minimizing Soret diffusion [*Sinmyo and Hirose*, 2010], and the flat-top geometry across the heating spot helps to achieve homogeneous heating. X-ray diffraction of annealed samples, was collected from the heating spot area after quenching from high temperature conditions. During laser heating the DACs were water cooled to prevent temperature-related drift of the DAC. Prior to XRD data collection the samples were centered on the vertical rotation axis orthogonal to the X-ray beam, and, thus, the sample detector distance was controlled and monitored to ensure reliable volume determination. The sample S2 was annealed for ~10 min only at the center of the sample after achieving the highest pressure, and sample S1 annealing was done at several pressures and several temperature steps with highest temperatures reaching ~2000–2200 K. Temperature was measured by fitting the black-body radiation collected from the heated spot to Planck's function [*Jeanloz and Heinz*, 1984; *Bassett and Weathers*, 1986].

X-ray diffraction analysis was performed using Fit2D [*Hammersley*, 1997] to integrate collected two-dimensional raw data into one dimension, and Fullprof [*Rodríguez-Carvajal*, 1993] and Unitcell [*Holland and Redfern*, 1997] software packages were used for volume determination. There is a good agreement between lattice parameters of individual phases determined by Fullprof and Unitcell.

3. Results

Below we present the experimental data on individual phase compression in a structured way. While the main focus of this paper is related to the spin state crossover of ferrous iron in the ferropericlase, we also show the compression behavior of Bm as the sample is a multiphase assemblage, and thus the interplay between phases which, we find, is important. This allows us to show similarities in behavior of these materials with different elastic properties being, on the one hand, part of the same sample and, on the other hand, being sintered to one another at all conditions of our studies.

3.1. X-Ray Diffraction

3.1.1. Analysis of XRD Patterns

For patterns collected at high pressures (Figure 3), we attribute all S1 XRD peaks to the phases Bm, Fp, and Ne, while S2 diffraction patterns contain additional peaks of Au-Pd from the multianvil capsule. No Au-Pd XRD peaks

were detected in S1 sample. We did not detect any $CaSiO_3$ XRD peaks in either sample at any pressure, likely due to the low abundance of Ca in the starting material (Table 2). Note the high abundance of Ne in both cases and a significant broadening of XRD peaks in S2 (relative to S1) even after sample annealing. We determined the volume as a function of pressure for Bm and Fp for S1 and S2 and present them below. We use Fp_{S1}, Fp_{S2}, Bm_{S1}, and Bm_{S2} abbreviations to distinguish phases belonging to each sample.

With respect to laser annealing and modification of diffraction pattern peak widths, we do not observe a significant decrease of individually resolved peak widths upon laser heating in S2 sample's central area, the same area used for our *P-V* data collection. Thus, the peak widths in S2 sample, namely, the sample at most nonhydrostatic compression, have not changed even under prolonged heating at ~2000 K. Additionally, the peak widths of the S1 sample, while not as wide as those in S2, were also not considerably affected by laser annealing.

3.1.2. Pressure, Normalized Stress, and Eulerian Strain

Normalized stress (F) was introduced as $F = P/[3f_E(1+2f_E)^{5/2}]$, where P represents pressure, $f_E(V) = 0.5[(V_0/V)^{2/3} - 1]$ is Eulerian strain, V is volume at a given pressure, and V_0 is a reference volume [*Birch*, 1978]. This term becomes widely used in combination with Birch-Murnaghan (BM) equation of state (EOS) analysis based on the assumption that Gibbs free energy for a given material is a polynomial function of Eulerian strain f_E [*Angel*, 2000]. The functional behavior of pressure P, bulk modulus K, and normalized stress F in a third-order truncation of BM EOS are given below:

$$P = 3K_0 f_E(1+2f_E)^{5/2}\left(1+1.5\left(K^{'}-4\right)f_E\right)K = K_0(1+2f_E)^{5/2}\left[1+\left(3K^{'}-5\right)f_E\right]F$$
$$= K_0 + 1.5K_0\left(K^{'}-4\right)f_E \quad (1)$$

where $K_0 = -V(\mathrm{d}P/\mathrm{d}V)_{P=0}$, $K' = (\mathrm{d}K/\mathrm{d}P)_{P=0}$ represent reference bulk modulus and bulk modulus pressure derivative, respectively. If we look closer at equation (1), we see that variation of normalized stress as a function of strain may reflect variations of K_0 or K', or both and, thus, may indicate a phase transition [*Maier et al*., 2011].

3.1.3. Detecting the Electron Spin State Crossover With XRD

After reviewing available literature data on iron spin state crossover in Fp and Bm, we find a change of normalized stress F as a function of strain f_E (e.g., Figure 4) for all data reporting in situ volume measurements. Moreover, this feature coincides both with a change of bulk and shear modulus as indicated in previous studies [*Marquardt et al*., 2009; *Chen et al*., 2012]. This feature highlighted by the black arrow in Figure 4 remains pronounced even if we plot normalized stress F as a function of pressure P (see Text S1, supporting information). Along similar lines, here we address some of the inconsistencies reported in the literature for Fp material with iron concentration $x = 0.17$ [*Lin et al*., 2005]. In Text S1 of supporting information, we present the original XRD data and show that spin state crossover region was originally misinterpreted.

It should be noted that our paper is not the first to mention the manifestation of HS-LS crossover on the F-f_E plot [i.e., see *Lin et al*., 2005; *Speziale et al*., 2007]. Some groups have even expanded this formal approach to a *G-g* plot. For the full discussion we point the interested reader to *Speziale et al*. [2007] and *Marquardt et al*. [2009]. For this work we employ the F-f_E framework since, first, it provides sufficient and more clear indication of spin state crossover even for small amount of iron, and, second, it provides a more obvious indication of deviatoric stress contribution and its annealing.

3.1.4. Detecting Features of Undesirable Stresses

XRD is also a powerful method to detect the evolution of undesirable stresses (Figure 4). Here we present F-f_E plots calculated from data obtained with XRD. In this figure, we compare data on similar Bm [*Catalli et al*., 2010, 2011] and Fp [*Lin et al*., 2005; *Mao et al*., 2011] compositions. Using dashed lines, we feature inconsistencies of material compressional behavior with ferrous or ferric iron in the low spin state (LS) visualized in the F-f_E plots. We find that a small difference in material chemistry cannot explain such strong variation of F. Here we are supported by our analysis of literature data (Text S1, supporting information) for Fp material with $x = 0.1$ [*Lin et al*., 2005; *Marquardt et al*., 2009; *Mao et al*., 2011], $x = 0.17$, and $x = 0.25$.

In order to explain higher than expected values of F indicated by gray star symbol in Figure 4 and high positive slope of dashed lines, we can use the following form of normalized stress:

$$F = \frac{P}{3f_E(1+2f_E)^{5/2}}$$

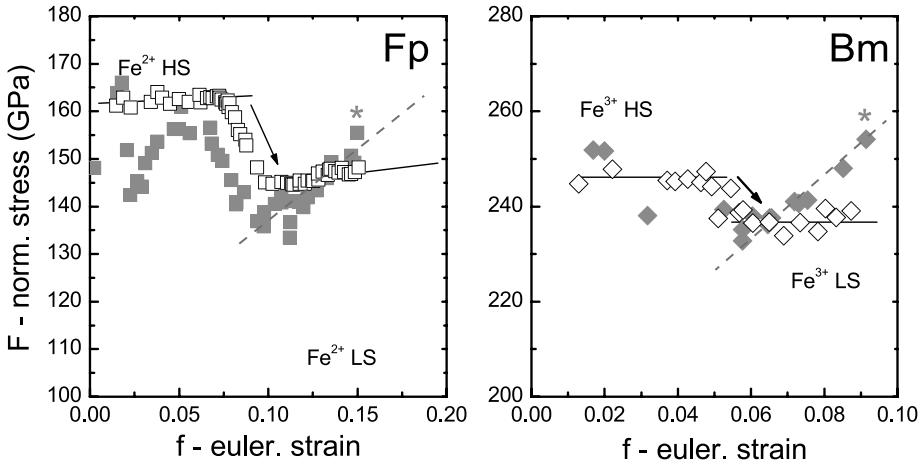

Figure 4. *F-f_E* plot for different Fp and Bm material reported in the literature. (left) Open square points represent Fp data ($x_{Fe} = 0.25$) [*Mao et al.*, 2011], and solid square points represent Fp data ($x_{Fe} = 0.17$) [*Lin et al.*, 2005]. The arrow indicates ferrous iron spin state crossover. Solid lines are guides for the eye featuring compressional behavior of open squares data before and after ferrous iron HS-LS crossover. Dashed line highlights behavior we attribute to the influence of undesirable stresses. (right) Compression of Bm enriched with Fe^{3+} reported in the literature. Data points (solid diamonds) represent Bm produced from $0.9MgSiO_3$,·$0.1Fe_2O_3$ glass [*Catalli et al.*, 2010] and (open diamonds) represent Bm produced from $0.90MgSiO_3$,·$0.05Al_2O_3$,·$0.05Fe_2O_3$ glass [*Catalli et al.*, 2011]. Solid lines are guides for the eye featuring two different trends of *F-f_E* behavior for Bm produced from glass containing Al. Similar to the case of ferrous iron HS-LS crossover in Fp, these lines should be attributed to Bm phases with different iron spin state. Arrow indicates spin state crossover of ferric iron. Additionally, it is also worth noting that the bulk modulus pressure derivative K' is close to the value of 4 (horizontal line, within the data scatter) for Al-bearing Bm with iron in HS and LS states. Dashed line highlights anomalous behavior we attribute to the influence of undesirable stresses. We infer that this behavior is due to unannealed undesirable stress components. For calculations of f_E and *F* values we employed V_0 values reported in the original publications. The slope of dashed lines (Figure 4, left and right) corresponds to $K' \sim 5.8$, which we consider an anomalously high value for both Bm and Fp phases. Gray star symbol indicates data points with highest pressure for gray filled symbols. For clarity, uncertainties are not shown. For *Lin et al.* [2005], *F* uncertainties range from ~±15 GPa at small f_E to ~ ±5 GPa at large f_E. For *Catalli et al.* [2010, 2011] *F* uncertainties are on the order of a few gigapascals. Additional information (i.e., error bars, if available) can be found in the original publications.

We suspect that the higher values of *F* correspond to incorrect measurements of pressure: the higher pressure measured inside the pressure chamber does not necessarily correspond to the actual pressure exerted on the sample. We attribute the mentioned anomalous behavior to the effect of undesirable stress in the sample in the uniaxial compressing geometry. In this case, the stress of the pressure medium transferring to the sample is unequally distributed between different stress tensor components in the sample giving rise to deviatoric stress and additionally enhancing the intergrain stress-strain interactions. We fully understand that this model is a simplified one; however, it serves an important first step toward our understanding of complex compression mechanics, including a deflection from a purely elastic behavior of the material.

We illustrate this idea using Figure 5 and the following analysis. Using definitions described in Figure 5, and following the procedure described in *Singh* [1993], for each point of the ideal pressure medium (PM), we can define the corresponding pressure P^{PM} as $P^{PM} = \sigma_{ii} = \sigma^{PM} = \Sigma\sigma_{ii}/3$; however, the stress tensor elements are different for the case of sample (SM) shown in the same figure. They are

$$\sigma_{ii}{}^{SM} = \sigma^{PM} - t, \quad i = 1, 2$$

$$\sigma_{ii}{}^{SM} = \sigma^{PM}, \quad i = 3$$

where *t* is uniaxial stress component [*Singh*, 1974, 1993; *Singh and Balasingh*, 1977]. Next, we find that equivalent hydrostatic pressure or mean normal stress of the sample (P^{SM}) has the following form:

$$P^{SM} = \frac{1}{3}\sum_i \sigma_{ii}{}^{SM} = \sigma^{PM} - \frac{2}{3}t < P^{PM}$$

This simple procedure shows that in case of evolving deviatoric stress affecting the stress state of the sample, the mean normal pressure of the sample (P^{SM}) is smaller than the mean normal pressure of the pressure

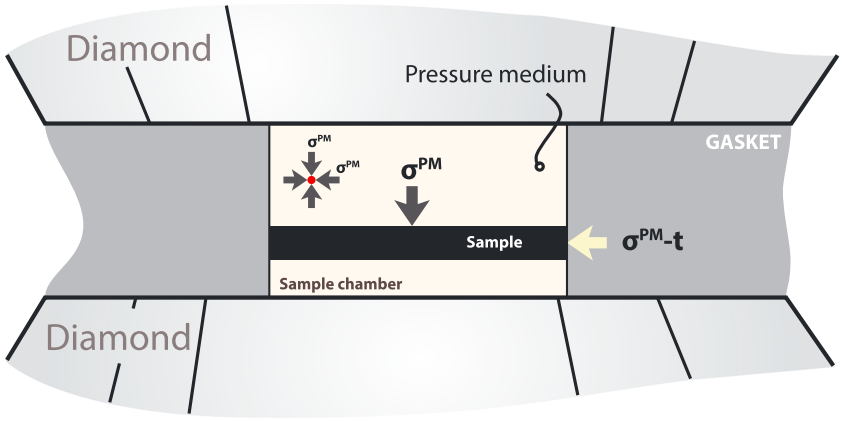

Figure 5. Stress diagram of DAC sample chamber in a uniaxial compression experiment. Following guidelines of the previously published analysis [*Singh*, 1993], we expect that for each individual infinitely small point of a model hydrostatic pressure medium (PM) illustrated by red point, the stress tensor components are equal to pressure $P^{PM} = \sigma_{ii} = \sigma^{PM} = \Sigma\sigma_{ii}/3 (i = 1, 2, 3)$, where $i = 3$ corresponds to the direction perpendicular the compressing diamond facet and $i = 1, 2$ correspond to the directions lying in plane of the facet. However, for the sample we have a different situation: $\sigma_{ii} = \sigma^{PM} - t$ for $i = 1, 2$ and $\sigma_{ii} = \sigma^{PM}$ for $i = 3$, with t introduced as the uniaxial stress component [*Singh*, 1974, 1993; *Singh and Balasingh*, 1977].

medium (P^{PM}). The latter one is detected by a pressure marker incorporated in the pressure medium, but not in the sample. From practical reasons, we can take a look at the same point from an alternative angle. Considering the effect of the hydrostatic and nonhydrostatic conditions (uniaxial stress) on material elasticity, at any given pressure reported by sensor in the pressure medium the compressed material should have larger volume in nonhydrostatic conditions.

For the sake of completeness, we also note another important contribution from undesirable stresses, namely, the intergrain microstress interactions. We find that it is almost impossible to see the corresponding effect in conventional high-pressure XRD experiments. In addition to pressure-induced contraction, individual crystals in a dense polycrystalline assemblage can also experience additional bulk compression or shear interactions with other grains, and, thus, we cannot exclude their indirect role for the modification of spin state crossover and its direct manifestation in XRD.

3.2. Laser Annealing and Undesirable Stresses

The laser heating technique has opened new horizons for material studies at extreme conditions. By creating high temperatures and boosting material kinetics including diffusion, laser heating has proved to be a powerful tool capable of stimulating phase formation from glasses [e.g., *Catalli et al*., 2010], capable of melting materials with very high melting temperature [*Boehler*, 1993; *Du and Lee*, 2014], and capable of reducing potential undesirable stresses [*Mao et al*., 2011; *Uts et al*., 2013].

It is clear that homogeneous annealing of the sample should decrease undesirable stresses occurring in the form of deviatoric stress or intergrain interactions by equilibrating thermodynamic environments of the sample and pressure medium. On a microscopic level this is efficiently achieved by reducing the number of intrinsic defects, such as dislocations created by compression as an equivalent of work hardening. We note that laser annealing may not reduce all undesirable stress contributions (e.g., pressure gradients, deviatoric stress, and grain-grain interactions); however, with proper selection of annealing conditions it should significantly reduce them as was demonstrated for solid pressure media [*Uts et al*., 2013].

Before we proceed with the discussion of collected XRD data, let us recall the differences between two different sample compression approaches: S1 and S2 (Figure 2). Although Ne is generally thought of as one of the best available pressure media [*Klotz et al*., 2009], the geometry of S2 suggests an evolution of nonhydrostatic conditions, including deviatoric stress. Such geometry of compression may additionally enhance grain-grain interactions promoting microstresses in the sample. The different hardnesses of Bm and Fp should enhance these effects even further. Here we observe a difference in peak profile widths for S1 and S2 samples at high pressure to illustrate this argument (Figure 3).

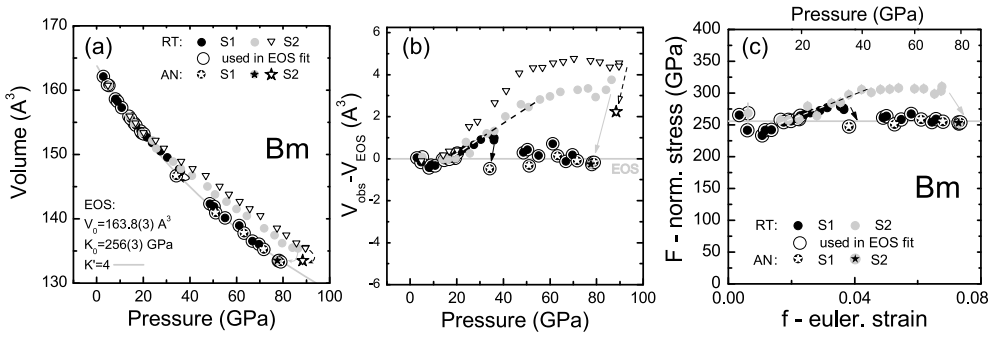

Figure 6. (a) Volume of Bm phase as a function of pressure collected at room temperature. Data points (black circles—Ne pressure scale) correspond to the Bm_{S1} (sample subjected to the most hydrostatic conditions), while triangles (Ne pressure scale) and gray circles (Au-Pd pressure scale) correspond to Bm_{S2}. Encircled points represent data taken into account for calculation of reference second-order Birch-Murnaghan equation of state (EOS—grey line). In the left lower corner of the plot we present the derived parameters (see text for discussion). By star symbols we indicate data points collected just after the sample laser annealing (AN). The difference between gray circles, triangles, and black points highlights effect of undesirable stresses relative to the most hydrostatic condition. (b) Difference between volume calculated using the Bm_{S1} EOS and actual experimental data. The horizontal line represents Bm_{S1} EOS, and arrows indicate effect of the first annealing for S1 and S2, respectively. Dashed lines in Figures 6b and 6c are guides for the eye showing similar behavior of black and gray points below 40 GPa and prior to the first laser heating of S1. These lines additionally highlight the effect of undesirable stresses. Please note a difference in *P-V* relations for S2 sample under consideration of Ne and Au-Pd pressure standard in the region prior to and upon the annealing indicated by the arrows. (c) F-f_E plots corresponding to Bm_{S1} and Bm_{S2}. Grey horizontal line in this plot corresponds to K_0 shown in the left figure. Pressure scales (in black) on the top of the plots were created according to the reference EOS function. Error bars are shown as vertical lines. Error bars are smaller or comparable with the corresponding symbol size (Figures 6a and 6b) and clearly visible in Figure 6c.

X-ray diffraction patterns (e.g., Figure 3) were collected at pressures up to 90 GPa (using Ne as a pressure scale) with and without laser annealing. In our study, we employ two approaches, namely, the sample S1 was annealed at several pressures above 36 GPa, while S2 was annealed only at the end of compression at ~90 GPa. We collected unit-cell volume data of Bm and Fp as a function of pressure, separately for S1 (reference hydrostatic conditions with suppression of undesirable stresses) and for S2 (nonhydrostatic conditions). The final annealing of S2 sample and comparison of the derived phase volumes with S1 phases serve as an additional check for consistency, as described below.

3.3. Compression of BM

First, we analyze data obtained for the Bm phase (Figure 6), the material with the highest volume fraction and at the same time the building frame of the sample. We take selected points of S1 (annealed, and thus, nearly hydrostatic conditions) and a few of S2 as a reference and calculate the equation of state (EOS) of the material using the points shown in Figure 6. Using a second-order Birch-Murnaghan equation of state [*Birch*, 1947], we obtain the following ambient conditions parameters, namely, volume $V_0 = 163.8(3)$ Å^3, bulk modulus $K_0 = 256(3)$ GPa, and pressure derivative of bulk modulus fixed to $K' = 4$, in good agreement with previous studies [e.g., *Saikia et al*., 2009]. The validity of our approach (fixing K') is supported by our analysis of normalized pressure (F) as a function of Eulerian strain (f_E) shown in the same figure.

While the composition of Bm for S1 and S2 is assumed to be the similar due to the same starting material, the stress conditions are different between samples. This can be clearly seen in Figure 6, where we present the Bm volume of S2 as a function of pressure using different pressure scales and the F-f_E plot. The difference between the Au-Pd pressure sensor (incorporated into the sample) and Ne surrounding S2 is clear and diverges as the pressure increases.

This observation requires some explanation. For sample S2, pressure is first transferred from the diamonds to the Ne and only then redistributed in the S2 sample into mean normal stress (hydrostatic component) and deviatoric and internal microstress components (e.g., intergrain). Au-Pd grains surrounded by hard Bm grains are also subjected to these stresses; however, Au-Pd, incorporated into the S2, is softer and plastic; thus, it could provide a better estimate of equivalent hydrostatic conditions inside the sample than Ne surrounding

the latter. Here and below, unless stated otherwise, data for S2 sample will be referenced to with Au-Pd pressure sensor.

Thus, prior to the laser heating, pressure derived from internal sensor Au-Pd should be closer to the mean normal stress of S2 sample than pressure derived from surrounding Ne. Even so, our data show that this pressure does not represent true mean normal stress, and we test and confirm this hypothesis by annealing the S2 material at the point of highest pressure.

Now, after annealing S2, we can test Au-Pd as pressure calibrant. This annealing is indicated by the thin gray arrow shown in the Figure 6. Here we see that the extracted *P-V* relation of Bm_{S2} becomes in agreement with *P-V* values of annealed Bm_{S1}. As will be shown later, we observe similar behavior for Fp. Thus, the observation that pressure measured by both Ne (P1) and Au-Pd (P2) for S2 (prior to laser annealing) is different from pressure close to hydrostatic (P3—annealed Bm_{S1}) cannot be explained by the presence of simple uniaxial stress component. We suggest that this difference between P1, P2, and P3 is the evidence for a complicated interaction between stresses on the macroscale and microscale. We add that we could not fully anneal the microstresses in the S2 sample because the width of the diffraction peaks did not change after the annealing.

We can also compare the deviations of Bm_{S1} and Bm_{S2} volumes from the estimated EOS as a function of pressure. Here by means of a dashed line we highlight an anomalous but similar behavior as these quantities deflect from the EOS at pressures below 36 GPa, namely, below the point of the first annealing of S1. This observation indicates an evolution of deviatoric stress even in the S1 material (prior to annealing), although the S1 sample is completely surrounded by Ne (Figure 2).

Thus, in order to get reliable EOS parameters for multiphase materials, special attention must be paid in order to reveal their true compressional behavior. While our study is not the first in highlighting the manifestation of nonhydrostatic conditions or the effect of pressure medium deviation from hydrostaticity [*Marquardt et al*., 2011; *Dorfman et al*., 2012; *Anzellini et al*., 2014; *Konôpková et al*., 2015], to the best of our knowledge, we are the first to highlight substantial complications in the case of multiphase materials (e.g., with phases welded one to another and/or with significant differences in elastic properties).

The dashed line shown in Figure 6b and featuring the basic evolution of undesirable stresses supports this statement. In our opinion it starts at pressures very close to the phase stability of Bm, and thus, at certain situations it will not be possible to anneal Bm. The situation becomes even less attractive if we consider the effect on Fp which we discuss later.

Analysis of the F-f_E supports our discussion, and we see that the first annealing of S1 sample reduces the magnitude of F, while f_E retains almost the same value. This is a direct example of uniaxial stress annealing. Following our discussion of F-f_E plots, by the annealing we produce a data point corresponding to the same volume or f_E but at lower pressure. This is similar to what was observed in other studies [e.g., *Marquardt et al*., 2011; *Anzellini et al*., 2014].

Finally, comparing our Bm data with literature (see also Figure 4), we do not see any other suspicious features in the F-f_E and ΔV plots of Bm_{S1} and Bm_{S2} phases. However, the scatter of our data for Bm phase prevents us from performing a reliable test for spin state crossover related to the incorporated ferric iron. The situation is also complicated with the multiphase state of our sample material (e.g., data of *Catalli et al*. [2010, 2011] are single phase), and with the fact that not every data point of the S1 sample has experienced annealing. In addition, if we consider our data on S2, we lack substantial evidence. Indeed, we do not know precisely the influence of the stresses on the microscale, as well as the influence of chemistry on the onset spin state crossover of ferric iron in Bm.

3.4. Compression of FP

We compute the Birch-Murnaghan second-order EOS for HS Fp taking selected Fp_{S1} and Fp_{S2} points as reference material (Figure 7). We report $V_0 = 76.3(1)$ Å^3, $K_0 = 163(5)$ GPa, and $K' = 4$ (fixed), in good agreement with previous studies [e.g., *Fei et al*., 2007a] for a similar starting composition.

First, we continue our analysis along similar lines as performed for Bm and highlight the effect of nonhydrostatic stresses appearing for Fp with a black dashed line (Figures 7b and 7c). A clear positive slope of this line and its intersection with the estimated EOS confirms that nonhydrostatic stresses start to evolve at pressures

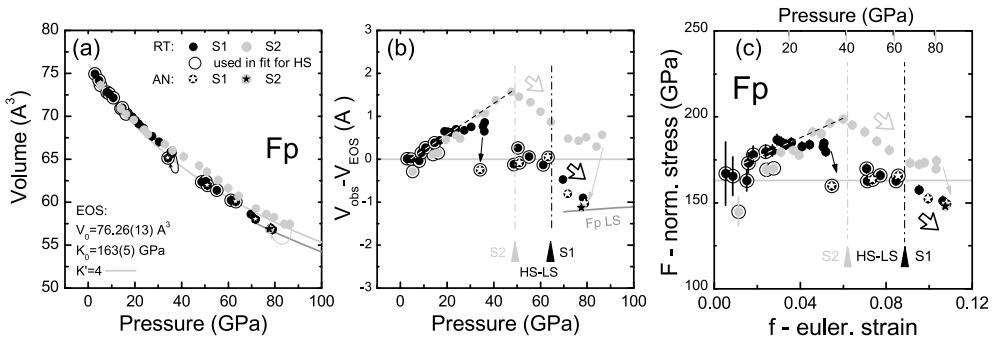

Figure 7. (a) Volume of Fp phase as a function of pressure collected at room temperature. Data points (black circles—Ne pressure scale) correspond to the Fp_{S1} (sample subjected to the most hydrostatic conditions) and gray circles (Au-Pd pressure scale) correspond to Fp_{S2}. Encircled points represent data taken into account for calculation of the second-order Birch-Murnaghan equation of state (grey line) for Fp_{S1} phase with corresponding high spin state of iron. By star symbols we indicate data points collected just after the sample laser annealing (AN). (b) Calculated difference between volume calculated using Fp EOS and actual experimental data. The horizontal line represents Fp_{S1} EOS, and arrows indicate effect of the first annealing. Vertical dash-dotted lines in Figures 7b and 7c highlight compression-induced volume collapse of Fp phase featuring ferrous iron HS-LS crossover in Fp_{S1} (black) and Fp_{S2} (gray). Bold arrows feature the direction of this process. Dark gray line shown in both Figures 7a and 7b is used as a reference. It corresponds to Fp ($x_{Fe} = 0.2$) with iron in low spin state [*Fei et al.*, 2007a]. Dashed lines in Figures 7b and 7c are guides for the eye showing similar behavior of black and gray points below prior to the first laser heating of S1. These lines highlight the effect of undesirable stresses. (c) F-f_E plots corresponding to Fp_{S1} and Fp_{S2}. Grey horizontal line in this plot corresponds to K_0 shown in the left figure. Pressure scales (in black) on the top of the plots were created according to the reference EOS function. The alternative grey pressure scale tick markers indicate pressures corresponding to the f_E values calculated with EOS parameters ($V_0 = 76.34A^3$ and $K_0 = 162$ GPa) reported previously for Fp material with similar starting composition $x_{Fe} = 0.25$ [*Mao et al.*, 2011]. Similar to Figure 7b, vertical dash-dotted lines indicate start of the HS-LS crossover for Fp_{S1} (hydrostatic conditions) and Fp_{S2} (nonhydrostatic conditions). Error bars are smaller or comparable with the corresponding symbol size (Figures 7a and 7b) and clearly visible in Figure 7c.

even lower than we expected for Bm, namely, much lower than 25 GPa, in the pressure region where we cannot anneal our sample due to Bm phase stability issue. This evidence becomes more pronounced in Figure 7b and affects our estimation of the Fp EOS.

This effect may also happen upon decompression since undesirable stresses evolve on both compression and decompression. As such, the data for multiphase materials collected on decompression also requires special attention and ideally good annealing.

Due to the complexity of this multiphase system, i.e., relative abundance of phases and their different elastic properties, the apparent pressure difference in the onset of undesirable stresses evolution for Fp and Bm (black dashed line in Figures 6b and 7b) further strengthens our argument for the complex interplay between macrostresses and microstresses and their distribution in a multiphase material.

Moving forward, we have demonstrated earlier that compression-driven volume collapse is a signature of Fe^{2+} HS-LS crossover in Fp. For a given pressure in the vicinity of HS-LS crossover in Fp, and depending on compositions, we expect a relative volume difference of 1–1.5 $Å^3$ between LS Fp and HS Fp for ambient temperature experiments [*Fei et al.*, 2007a; *Mao et al.*, 2011]. Here we report a clear manifestation of pressure-induced HS-LS crossover in samples Fp_{S1} and Fp_{S2} and demonstrate it by the vertical dashed lines in Figures 7b and 7c.

4. Discussion

Focusing on spin state crossover in Fp, we note that we can rely on *P-V* relations measured for annealed S1 sample, including the critical values of *P*, *V*, and f_E corresponding to the onset of crossover. However, with respect to the S2 sample, we only have reliable data on volume. Still, by knowing the *P-V* relation for the material with similar composition [e.g., *Mao et al.*, 2011], we can recalculate values of *P* corresponding to our values of Fp_{S2} *V*. This approach is further supported by estimation of our EOS parameters and their comparison with literature. We compare values of *P* calculated with our and *Mao et al.* [2011] EOS in the upper axis of Figure 7c and find that the margin is minimal. However, for the reference we will rely on data provided by the published model [*Mao et al.*, 2011]. Thus, we

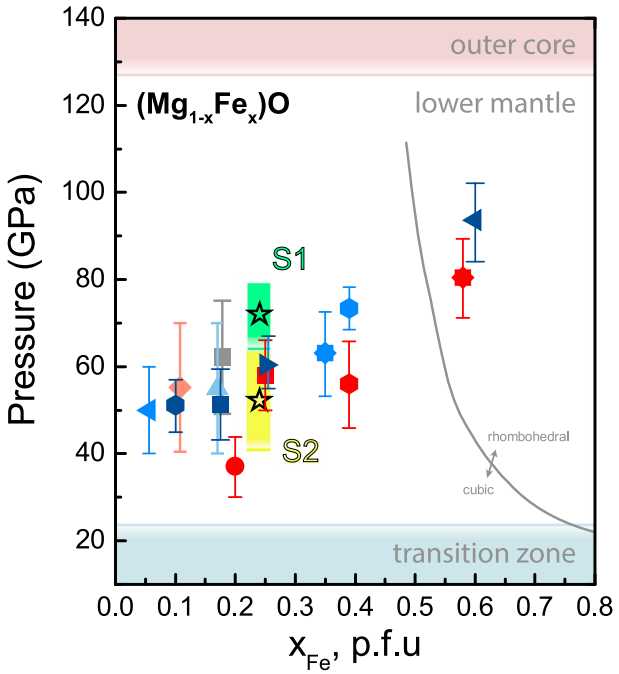

Figure 8. Updated phase diagram of ferropericlase ($Mg_{1-x}Fe_xO$) demonstrating our and the literature data on spin state crossover. All data points were measured at room temperature. Error bar symbols correspond to the apparent width of the transition as introduced and discussed in the supporting information. Symbol descriptions are the same as in Figure 1. The green and bright yellow regions indicate spin state crossover regions as determined for Fp_{S1} (hydrostatic conditions) and Fp_{S2} (strictly nonhydrostatic conditions), respectively.

can reconstruct the full *P-V* space for HS Fp_{S2} and determine the critical pressure corresponding to the onset of HS-LS transition. We combine our data with literature in Figure 8.

From Figure 8 it becomes clear that HS-LS crossover occurs at higher pressures for S1 (green) and lower pressures for S2 (yellow) when compared with the results of *Mao et al.* [2011] (red square) and *Lin et al.* [2005] (dark blue right triangle). Below we try to address both observations.

The annealed Fp_{S1} has undergone significant number of annealing events. Heating may induce a change in chemistry, e.g., through repartitioning of iron between Bm and Fp. The partitioning coefficient (K_D) may vary as a function of pressure and temperature [e.g., *Nakajima et al.*, 2012], and the situation becomes further complicated if we consider the additional effect of the HS-LS crossover [*Irifune et al.*, 2010]. Together these effects should enrich the Fp phase with iron further, thus shifting the onset of the crossover to higher pressures and enlarging its width. In this case Fp_{S1} would have a greater concentration of iron, and the Fp EOS which we obtained will correspond to a convolution of different Fp EOS with varying Fe content reflecting the changes of K_D.

However, from the paper of *Nakajima et al.* [2012] we see that modifications of our K_D for Fp_{S1} in our case should not be significant. There is very limited capacity for incorporation of ferric iron inside Fp, and most changes will be caused by changes in the ferrous iron. Most of the experimental work on iron partitioning has significant room for uncertainty. Thus, this effect should play a less important role in our observations.

A more likely explanation for the observation is as follows. There is general agreement that for Fp with iron content similar to ours, $x_{Fe} = 0.24(2)$, the Clapeyron slope of HS-LS transition is positive [*Mao et al.*, 2011; *Holmström and Stixrude*, 2015]. Now if our material (ambient temperature) is in the vicinity of the crossover with low abundance of LS state, heating of the pure material will convert LS into HS state. Quenching of the pure phase with the given ideal hydrostatic conditions and significant time for relaxation will promote reappearance of the same portion for the LS state. However, in our case of clearly nonhydrostatic conditions and densely sintered Bm and Fp multiphase assemblage, we can expect modification of the HS-LS stability region into a metastable one stimulating the stabilization of HS state. We suggest that this is only possible at low abundance of LS component, and at a certain pressure range, depending on composition. Sufficient heating will be indeed capable of fully converting the present LS state.

With respect to the Fp_{S2} we propose a different scenario. Here we have data collected on cold compression and no laser heating. Using our approach to reconstruct *P-V* space of Fp_{S2}, we effectively remove all contributions from the uniaxial macrostress component. Still, we see that the spin state transition happens at lower pressures than expected. Suspiciously, it moves in the direction reported for *Fei et al.* [2007a] point (red circle, similar composition).

While we have efficiently extracted the contribution from macrostresses from our Fp_{S2} data, we still have a significant contribution from microstrains and the related stresses. The evidence for this is the large peak width

on the corresponding diffraction patterns (Figure 3). These microstresses are likely responsible for our observations, and we suggest that they can explain the apparent deflection of *Fei et al*. [2007a] data from other literature.

In our case of enhanced nonhydrostaticity and a multiphase material, these contributions on the microlevel can lead to rhombohedral distortions of Fp material. These distortions could be well hidden within the broad peak widths of the S2 diffraction patterns. It is known that such distortions are typical for Fp as a single-phase material at nonhydrostatic conditions. They stimulate the appearance of the spin state crossover at lower pressures by modifying the ideal cubic environment of the ferrous iron [*Burns*, 2005]. In our case, this modification shifts the critical pressures of the HS-LS transition to the lower pressure region. The laser annealing has reduced the uniaxial stress component producing correct *P-V* values; however, the width of the peaks remained unchanged. This observation suggests that in order to anneal the microstresses in our Fp_{S2}, we have to overcome a significant energy barrier.

Although we demonstrate this effect for a complex, strongly nonhydrostatic system, this effect can also explain the differences between the three data points shown in Figure 8 at $x = 0.4$ [*Fei et al*., 2007a; *Zhuravlev et al*., 2009; *Chen et al*., 2012]. The experiments of *Zhuravlev et al*. [2009] and *Chen et al*. [2012] were conducted using the same pressure medium (neon) without any annealing. The experiments by *Fei et al*. [2007a], however, used NaCl and were laser annealed.

5. Conclusions

In our experiments we try to understand various phenomena appearing during the compression of a dense multiphase assemblage with composition resembling the lower mantle. In particular, we address inconsistencies in the ambient temperature Fp spin state crossover phase diagram. This diagram can be used as a starting point for thermodynamical calculations simulating conditions of the planetary interiors.

We compress two samples of the same well-characterized bulk starting composition in a diamond anvil cell experiment. However, one of them is subjected to nearly hydrostatic conditions (S1), while the geometry of the other promotes strongly nonhydrostatic conditions (S2). We have revealed the complexity of such a system with a strong interplay between uniaxial stress and microstrain components. In particular, we have demonstrated that undesirable stresses evolve more pronouncedly in multiphase assemblages as compared to a single-phase material, at least for an unbridged material fully surrounded by one of the most hydrostatic pressure media. We focus on these phenomena using both an internal (i.e., Au-Pd is intermixed with sample) and an external (i.e., Ne surrounds the sample) pressure standard.

Using our data on material density, we highlight two possible scenarios of how nonhydrostatic conditions affect our understanding of the Fp spin state crossover. The first one is connected with the incapability to measure pressure inside the sample. This leads to pressure overestimation. Although, this effect was already covered in the literature [e.g., *Marquardt et al*., 2011], we take a closer look at individual phases in a multiphase assemblage.

The second scenario is connected with the evolution of microstresses (e.g., intergrain) and with the effect of the reduction of starting pressures of ferrous iron spin state crossover. We discuss the inconsistencies existing in the literature, especially for previously reported Fp compositions with iron concentrations relevant for the lower mantle.

Finally, our analysis paves the way for a better understanding of multiphase compression. This is an important step for a better understanding of high-pressure experiments in general and the deep Earth related studies in particular.

Acknowledgments
This work was funded by NSF (grant EAR-0955824). Experiments were performed at HPCAT (Sector 16), Advanced Photon Source (APS), Argonne National Laboratory. HPCAT operations are supported by DOE-NNSA under award DE-NA0001974 and DOE-BES under award DE-FG02-99ER45775, with partial instrumentation funding by NSF. APS is supported by DOE-BES, under contract DE-AC02-06CH11357. Ne pressure medium loading was performed at GeoSoilEnviroCARS (Sector 13), Advanced Photon Source (APS), Argonne National Laboratory. GeoSoilEnviroCARS is supported by the National Science Foundation-Earth Sciences (EAR-1128799) and Department of Energy-Geosciences (DE-FG02-94ER14466). Use of the Advanced Photon Source was supported by the U.S. Department of Energy, Office of Science, Office of Basic Energy Sciences, under contract DE-AC02-06CH11357. This research was partially supported by COMPRES, the Consortium for Materials Properties Research in Earth Sciences, under NSF cooperative agreement EAR 11–57758. We acknowledge Shun-ichiro Karato for his assistance and advice, which improved the manuscript, and Catherine McCammon for Mössbauer measurements. We acknowledge the technical assistance of George Amulele, Chris Fiederlein, and Bill Samela. The requests for data should be directed to konstantin.glazyrin@gmail.com. We acknowledge the help of Bayerisches Geoinstitut staff for the initial TEM sample preparation (Hubert Schulze) and Mössbauer data collection (Catherine McCammon).

References

Angel, R. J. (2000), Equations of state, in *High-Temperature and High Pressure Crystal Chemistry, MSA, Reviews in Mineralogy and Geochemistry*, vol. 41, edited by R. M. Hazen and R. T. Downs, pp. 35–60, Mineralog. Soc. of Am., Washington, D. C.

Antonangeli, D., J. Siebert, C. M. Aracne, D. L. Farber, A. Bosak, M. Hoesch, M. Krisch, F. J. Ryerson, G. Fiquet, and J. Badro (2011), Spin crossover in ferropericlase at high pressure: A seismologically transparent transition?, *Science*, *331*(6013), 64–67, doi:10.1126/science.1198429.

Anzellini, S., A. Dewaele, F. Occelli, P. Loubeyre, and M. Mezouar (2014), Equation of state of rhenium and application for ultra high pressure calibration, *J. Appl. Phys.*, *115*(4), 043511, doi:10.1063/1.4863300.

Badro, J., G. Fiquet, F. Guyot, J.-P. Rueff, V. V. Struzhkin, G. Vankó, and G. Monaco (2003), Iron partitioning in Earth's mantle: Toward a deep lower mantle discontinuity, *Science*, *300*(5620), 789–791, doi:10.1126/science.1081311.

Bassett, W., and M. Weathers (1986), Temperature measurement in laser heated diamond anvil cells, *Physica B+C*, *139–140*, 900–902, doi:10.1016/0378-4363(86)90724-2.

Bina, C. R. (2005), Seismological constraints upon mantle composition, in *Treatise on Geochemistry: The Mantle and Core*, edited by R. W. Carlson, pp. 39–59, Elsevier, Oxford.
Birch, F. (1947), Finite elastic strain of cubic crystals, *Phys. Rev.*, *71*(11), 809–824, doi:10.1103/PhysRev.71.809.
Birch, F. (1978), Finite strain isotherm and velocities for single-crystal and polycrystalline NaCl at high pressures and 300°K, *J. Geophys. Res.*, *83*(B3), 1257–1268, doi:10.1029/JB083iB03p01257.
Boehler, R. (1993), Temperatures in the Earth's core from melting-point measurements of iron at high static pressures, *Nature*, *363*(6429), 534–536, doi:10.1038/363534a0.
Burns, R. (2005), *Mineralogical Applications of Crystal Field Theory*, 2nd ed., Cambridge Univ. Press, Cambridge.
Catalli, K., S.-H. Shim, V. B. Prakapenka, J. Zhao, W. Sturhahn, P. Chow, Y. Xiao, H. Liu, H. Cynn, and W. J. Evans (2010), Spin state of ferric iron in MgSiO3 perovskite and its effect on elastic properties, *Earth Planet. Sci. Lett.*, *289*(1–2), 68–75, doi:10.1016/j.epsl.2009.10.029.
Catalli, K., S.-H. Shim, P. Dera, V. B. Prakapenka, J. Zhao, W. Sturhahn, P. Chow, Y. Xiao, H. Cynn, and W. J. Evans (2011), Effects of the Fe^{3+} spin transition on the properties of aluminous perovskite—New insights for lower-mantle seismic heterogeneities, *Earth Planet. Sci. Lett.*, *310*(3–4), 293–302, doi:10.1016/j.epsl.2011.08.018.
Chen, B., J. M. Jackson, W. Sturhahn, D. Zhang, J. Zhao, J. K. Wicks, and C. A. Murphy (2012), Spin crossover equation of state and sound velocities of (Mg 0.65 Fe 0.35)O ferropericlase to 140 GPa, *J. Geophys. Res.*, *117*, B08208, doi:10.1029/2012JB009162.
Crowhurst, J. C., J. M. Brown, A. F. Goncharov, and S. D. Jacobsen (2008), Elasticity of (Mg,Fe)O through the spin transition of iron in the lower mantle, *Science*, *319*(5862), 451–453, doi:10.1126/science.1149606.
Dorfman, S. M., V. B. Prakapenka, Y. Meng, and T. S. Duffy (2012), Intercomparison of pressure standards (Au, Pt, Mo, MgO, NaCl and Ne) to 2.5 Mbar, *J. Geophys. Res.*, *117*, B08210, doi:10.1029/2012JB009292.
Du, Z., and K. K. M. Lee (2014), High-pressure melting of MgO from (Mg,Fe)O solid solutions, *Geophys. Res. Lett.*, *41*, 8061–8066, doi:10.1002/2014GL061954.
Dziewonski, A. M., and D. L. Anderson (1981), Preliminary reference Earth model, *Phys. Earth Planet. Inter.*, *25*(4), 297–356, doi:10.1016/0031-9201(81)90046-7.
Fei, Y., L. Zhang, A. Corgne, H. Watson, A. Ricolleau, Y. Meng, and V. Prakapenka (2007a), Spin transition and equations of state of (Mg, Fe)O solid solutions, *Geophys. Res. Lett.*, *34*, L17307, doi:10.1029/2007GL030712.
Fei, Y., A. Ricolleau, M. Frank, K. Mibe, G. Shen, and V. Prakapenka (2007b), Toward an internally consistent pressure scale, *Proc. Natl. Acad. Sci. U.S.A.*, *104*(22), 9182–9186, doi:10.1073/pnas.0609013104.
Hammersley, A. P. (1997), Fit2D. An introduction and overview, *ESRF Intern. Rep.*, *ESRF97HA02*.
Holland, T. J. B., and S. A. T. Redfern (1997), Unit cell refinement from powder diffraction data; the use of regression diagnostics, *Mineral. Mag*, *61*(1), 65–77.
Holmström, E., and L. Stixrude (2015), Spin crossover in ferropericlase from first-principles molecular dynamics, *Phys. Rev. Lett.*, *114*(11), 117202, doi:10.1103/PhysRevLett.114.117202.
Hsu, H., K. Umemoto, P. Blaha, and R. M. Wentzcovitch (2010), Spin states and hyperfine interactions of iron in (Mg,Fe)SiO3 perovskite under pressure, *Earth Planet. Sci. Lett.*, *294*(1–2), 19–26, doi:10.1016/j.epsl.2010.02.031.
Irifune, T., T. Shinmei, C. A. McCammon, N. Miyajima, D. C. Rubie, and D. J. Frost (2010), Iron partitioning and density changes of pyrolite in Earth's lower mantle, *Science*, *327*(5962), 193–195, doi:10.1126/science.1181443.
Javoy, M., et al. (2010), The chemical composition of the Earth: Enstatite chondrite models, *Earth Planet. Sci. Lett.*, *293*(3–4), 259–268, doi:10.1016/j.epsl.2010.02.033.
Jeanloz, R., and D. L. Heinz (1984), Experiments at high temperature and pressure: Laser heating through the diamond cell, *J. Phys. Colloq.*, *45*, 83–92, doi:10.1051/jphyscol:1984817.
Kantor, A., S. Jacobsen, I. Kantor, L. Dubrovinsky, C. McCammon, H. Reichmann, and I. Goncharenko (2004), Pressure-induced magnetization in FeO: Evidence from elasticity and Mössbauer spectroscopy, *Phys. Rev. Lett.*, *93*(21), doi:10.1103/PhysRevLett.93.215502.
Klotz, S., J. C. Chervin, P. Munsch, and G. Le Marchand (2009), Hydrostatic limits of 11 pressure transmitting media, *J. Phys. D Appl. Phys.*, *42*, 075413, doi:10.1088/0022-3727/42/7/075413.
Kobayashi, Y. (2005), Fe-Mg partitioning between (Mg, Fe)SiO 3 post-perovskite, perovskite, and magnesiowüstite in the Earth's lower mantle, *Geophys. Res. Lett.*, *32*, L19301, doi:10.1029/2005GL023257.
Konôpková, Z., A. Rothkirch, A. K. Singh, S. Speziale, and H.-P. Liermann (2015), In situ X-ray diffraction of fast compressed iron: Analysis of strains and stress under non-hydrostatic pressure, *Phys. Rev. B*, *91*(14), 144101, doi:10.1103/PhysRevB.91.144101.
Lee, K. K. M., B. O'Neill, W. R. Panero, S.-H. Shim, L. R. Benedetti, and R. Jeanloz (2004), Equations of state of the high-pressure phases of a natural peridotite and implications for the Earth's lower mantle, *Earth Planet. Sci. Lett.*, *223*(3–4), 381–393, doi:10.1016/j.epsl.2004.04.033.
Lin, J.-F., V. V. Struzhkin, S. D. Jacobsen, M. Y. Hu, P. Chow, J. Kung, H. Liu, H.-K. Mao, and R. J. Hemley (2005), Spin transition of iron in magnesiowüstite in the Earth's lower mantle, *Nature*, *436*(7049), 377–380, doi:10.1038/nature03825.
Lin, J.-F., S. Speziale, Z. Mao, and H. Marquardt (2013), Effects of the electronic spin transitions of iron in lower mantle minerals: Implications for deep mantle geophysics and geochemistry, *Rev. Geophys.*, *51*, 244–275, doi:10.1002/rog.20010.
Maier, B. J., et al. (2011), Effect of La doping on the ferroic order in Pb-based perovskite-type relaxor ferroelectrics, *Phys. Rev. B*, *83*(13), 134106, doi:10.1103/PhysRevB.83.134106.
Mao, H. K., J. Xu, and P. M. Bell (1986), Calibration of the ruby pressure gauge to 800 kbar under quasi-hydrostatic conditions, *J. Geophys. Res.*, *91*(B5), 4673–4676, doi:10.1029/JB091iB05p04673.
Mao, Z., J.-F. Lin, J. Liu, and V. B. Prakapenka (2011), Thermal equation of state of lower-mantle ferropericlase across the spin crossover, *Geophys. Res. Lett.*, *38*, L23308, doi:10.1029/2011GL049915.
Marquardt, H., S. Speziale, H. J. Reichmann, D. J. Frost, and F. R. Schilling (2009), Single-crystal elasticity of $(Mg_{0.9}Fe_{0.1})O$ to 81 GPa, *Earth Planet. Sci. Lett.*, *287*(3–4), 345–352, doi:10.1016/j.epsl.2009.08.017.
Marquardt, H., S. Speziale, K. Marquardt, H. J. Reichmann, Z. Konôpková, W. Morgenroth, and H.-P. Liermann (2011), The effect of crystallite size and stress condition on the equation of state of nanocrystalline MgO, *J. Appl. Phys.*, *110*(11), 113512, doi:10.1063/1.3662491.
McCammon, C. (1992), A new apparatus to conduct variable temperature high pressure Mössbauer spectroscopy, in *Recent Trends in High Pressure Research (Proceedings of the XIII AIRAPT International Conference on High Pressure Science and Technology)*, edited by A. K. Singh, pp. 824–826, Oxford and IBL Publ. Co., New Delhi, India.
Meng, Y., G. Shen, and H.-K. Mao (2006), Double-sided laser heating system at HPCAT for in situ X-ray diffraction at high pressures and high temperatures, *J. Phys. Condens. Matter*, *18*(25), S1097–S1103, doi:10.1088/0953-8984/18/25/S17.
Nakajima, Y., D. J. Frost, and D. C. Rubie (2012), Ferrous iron partitioning between magnesium silicate perovskite and ferropericlase and the composition of perovskite in the Earth's lower mantle, *J. Geophys. Res.*, *117*, B08201, doi:10.1029/2012JB009151.

Otsuka, K., C. A. McCammon, and S. Karato (2010), Tetrahedral occupancy of ferric iron in (Mg,Fe)O: Implications for point defects in the Earth's lower mantle, *Phys. Earth Planet. Inter.*, *180*(3–4), 179–188, doi:10.1016/j.pepi.2009.10.005.

Potapkin, V., et al. (2013), Effect of iron oxidation state on the electrical conductivity of the Earth's lower mantle, *Nat. Commun.*, *4*, 1427, doi:10.1038/ncomms2436.

Ringwood, A. (1975), *Composition and Petrology of the Earth's Mantle*, McGraw-Hill, New York.

Rodríguez-Carvajal, J. (1993), Recent advances in magnetic structure determination by neutron powder diffraction, *Phys. B Condens. Matter*, *192*(1–2), 55–69, doi:10.1016/0921-4526(93)90108-I.

Saikia, A., T. B. Ballaran, and D. J. Frost (2009), The effect of Fe and Al substitution on the compressibility of $MgSiO_3$-perovskite determined through single-crystal X-ray diffraction, *Phys. Earth Planet. Inter.*, *173*(1–2), 153–161, doi:10.1016/j.pepi.2008.11.006.

Shimizu, H., H. Imaeda, T. Kume, and S. Sasaki (2005), High-pressure elastic properties of liquid and solid neon to 7 GPa, *Phys. Rev. B*, *71*(1), 014108, doi:10.1103/PhysRevB.71.014108.

Singh, A. K. (1974), Uniaxial stress component in tungsten carbide anvil high-pressure X-ray cameras, *J. Appl. Phys.*, *45*(11), 4686, doi:10.1063/1.1663119.

Singh, A. K. (1993), The lattice strains in a specimen (cubic system) compressed nonhydrostatically in an opposed anvil device, *J. Appl. Phys.*, *73*(9), 4278, doi:10.1063/1.352809.

Singh, A. K., and C. Balasingh (1977), Uniaxial stress component in diamond anvil high-pressure X-ray cameras, *J. Appl. Phys.*, *48*(12), 5338, doi:10.1063/1.323568.

Sinmyo, R., and K. Hirose (2010), The Soret diffusion in laser-heated diamond-anvil cell, *Phys. Earth Planet. Inter.*, *180*(3–4), 172–178, doi:10.1016/j.pepi.2009.10.011.

Speziale, S., V. E. Lee, S. M. Clark, J. F. Lin, M. P. Pasternak, and R. Jeanloz (2007), Effects of Fe spin transition on the elasticity of (Mg, Fe)O magnesiowüstites and implications for the seismological properties of the Earth's lower mantle, *J. Geophys. Res.*, *112*, B10212, doi:10.1029/2006JB004730.

Sturhahn, W., J. M. Jackson, and J.-F. Lin (2005), The spin state of iron in minerals of Earth's lower mantle, *Geophys. Res. Lett.*, *32*, L12307, doi:10.1029/2005GL022802.

Tschauner, O., C. Ma, J. R. Beckett, C. Prescher, V. B. Prakapenka, and G. R. Rossman (2014), Mineralogy. Discovery of bridgmanite, the most abundant mineral in Earth, in a shocked meteorite, *Science*, *346*(6213), 1100–1102, doi:10.1126/science.1259369.

Uts, I., K. Glazyrin, and K. K. M. Lee (2013), Effect of laser annealing of pressure gradients in a diamond-anvil cell using common solid pressure media, *Rev. Sci. Instrum.*, *84*, 103904, doi:10.1063/1.4821620.

van Aken, P. A., and B. Liebscher (2002), Quantification of ferrous/ferric ratios in minerals: New evaluation schemes of Fe L_{23} electron energy-loss near-edge spectra, *Phys. Chem. Miner.*, *29*(3), 188–200, doi:10.1007/s00269-001-0222-6.

Van Cappellen, E. (1990), The parameterless correction method in X-ray microanalysis, *Microsc. Microanal. Microstruct.*, *1*(1), 1–22, doi:10.1051/mmm:01990001010100.

Van Cappellen, E., and J. C. Doukhan (1994), Quantitative transmission X-ray microanalysis of ionic compounds, *Ultramicroscopy*, *53*(4), 343–349, doi:10.1016/0304-3991(94)90047-7.

Xu, W., C. Lithgow-Bertelloni, L. Stixrude, and J. Ritsema (2008), The effect of bulk composition and temperature on mantle seismic structure, *Earth Planet. Sci. Lett.*, *275*(1–2), 70–79, doi:10.1016/j.epsl.2008.08.012.

Zhuravlev, K. K., J. M. Jackson, A. S. Wolf, J. K. Wicks, J. Yan, and S. M. Clark (2009), Isothermal compression behavior of (Mg,Fe)O using neon as a pressure medium, *Phys. Chem. Miner.*, *37*(7), 465–474, doi:10.1007/s00269-009-0347-6.